Molecular and Cellular Biochemistry
https://doi.org/10.1007/s11010-020-03809-4

dSTORM microscopy evidences in HeLa cells clustered and scattered γH2AX nanofoci sensitive to ATM, DNA-PK, and ATR kinase inhibitors

Pablo Liddle[1] · Jorge Jara-Wilde[2,3] · Laura Lafon-Hughes[1] · Iván Castro[2] · Steffen Härtel[2,4] · Gustavo Folle[1]

Received: 31 December 2019 / Accepted: 18 June 2020

Abstract

In response to DNA double-strand breaks (DSB), histone H2AX is phosphorylated around the lesion by a feed forward signal amplification loop, originating γH2AX foci detectable by immunofluorescence and confocal microscopy as elliptical areas of uniform intensity. We exploited the significant increase in resolution (~×10) provided by single-molecule localization microscopy (SMLM) to investigate at nanometer scale the distribution of γH2AX signals either endogenous (controls) or induced by the radiomimetic bleomycin (BLEO) in HeLa cells. In both conditions, clustered substructures (nanofoci) confined to γH2AX foci and scattered nanofoci throughout the remnant nuclear area were detected. SR-Tesseler software (Voronoï tessellation-based segmentation) was combined with a custom Python script to first separate clustered nanofoci inside γH2AX foci from scattered nanofoci, and then to perform a cluster analysis upon each nanofoci type. Compared to controls, γH2AX foci in BLEO-treated nuclei presented on average larger areas (0.41 versus 0.19 μm^2), more nanofoci per focus (22.7 versus 13.2) and comparable nanofoci densities (~60 nanofoci/μm^2). Scattered γH2AX nanofoci were equally present (~3 nanofoci/μm^2), suggesting an endogenous origin. BLEO-treated cells were challenged with specific inhibitors of canonical H2AX kinases, namely: KU-55933, VE-821 and NU-7026 for ATM, ATR and DNA-PK, respectively. Under treatment with pooled inhibitors, clustered nanofoci vanished from super-resolution images while scattered nanofoci decreased (~50%) in density. Residual scattered nanofoci could reflect, among other alternatives, H2AX phosphorylation mediated by VRK1, a recently described non-canonical H2AX kinase. In addition to H2AX findings, an analytical approach to quantify clusters of highly differing density from SMLM data is put forward.

Keywords DNA damage · γH2AX nanofoci · ATM/ATR/DNA-PK inhibitors · SMLM microscopy · Voronoï tessellation

Abbreviations

γH2AX	Histone H2AX phosphorylated on serine 139
ATM	Ataxia telangiectasia mutated
ATR	ATM and Rad3-related
BLEO	Bleomycin
CLSM	Confocal laser scanning microscopy
DDR	DNA damage response
DNA-PK	DNA-dependent protein kinase
DSB	Double-strand break
dSTORM	Direct stochastic optical reconstruction microscopy
IR	Ionizing radiation
LET	Linear energy transfer
MAPK	Mitogen-activated protein kinase
PI3K	Phosphatidylinositol 3-kinase
ROI	Region of interest
SIM	Structured illumination microscopy
SMLM	Single-molecule localization microscopy
STED	Stimulated emission depletion microscopy
TSS	Transcription start site

Electronic supplementary material The online version of this article (https://doi.org/10.1007/s11010-020-03809-4) contains supplementary material, which is available to authorized users.

✉ Pablo Liddle
pabloliddle@gmail.com

[1] Departamento de Genética, Instituto de Investigaciones Biológicas Clemente Estable, Montevideo, Uruguay

[2] SCIAN-Lab, Biomedical Neuroscience Institute (BNI), Santiago, Chile

[3] Departamento de Ciencias de la Computación, Universidad de Chile, Santiago, Chile

[4] Instituto de Ciencias Biomédicas, Facultad de Medicina, Universidad de Chile, Santiago, Chile

Published online: 07 July 2020

Introduction

Cells respond to DNA damage by activating a complex set of biochemical signaling pathways, known as the DNA damage response (DDR), which aims to restore DNA integrity and maintain genomic stability. Critical regulators of the DDR are remodeling and chromatin-modifying activities. A very important chromatin modification in response to DNA double-strand breaks, DSB [1] or stalled replication forks [2] is the phosphorylation of the histone H2A variant H2AX on a conserved C-terminal serine residue, generating γH2AX. The phosphorylation begins few minutes after DNA damage induction, reaches a maximum (plateau) 15–60 min later, and decays steadily afterwards [3]. It spreads 1–2 Mb around the lesion, allowing immunodetection as microscopically visible (Ø ~ 0.4–1.0 μm) γH2AX foci by standard fluorescence microscopy [4]. Although the presence of γH2AX is not required for initial damage recognition, it is critical for the efficient recruitment and/or retention of DNA repair factors at the lesion site thus amplifying the DNA damage signaling [5]. Phosphorylation of H2AX to γH2AX in the surroundings of lesion sites is mediated by ATM (ataxia telangiectasia mutated), ATR (ATM and Rad3-related) and DNA-PK (DNA-dependent protein kinase), which are members of the PI3K (phosphatidylinositol 3-kinases) family of protein kinases. ATM and DNA-PK phosphorylate H2AX in response to directly induced DSB, while at stalled forks generated during replication stress, H2AX phosphorylation is primarily mediated by ATR [2].

DSB are the most critical DNA lesion since they directly compromise genome integrity. If the lesion is left partially or entirely unrepaired, it can trigger cell death or lead to chromosome breaks and translocations related with human diseases and cancer proneness [6]. Endogenous processes, such as DNA replication [7], transcription [8], 3D genome folding [9] or V(D)J recombination in developing thymocytes [10] can induce DSB. Additionally, DSB can be induced by physical (mainly ionizing radiations, IR) and chemical agents (known as radiomimetics) which are able to insult DNA by a direct free radical attack on the deoxyribose backbone.

Bleomycin (BLEO) is a radiomimetic chemical isolated from *Streptomyces verticillus* [11] that consists of a closely related family of glycopeptides. By means of a 5′-G-Py-3′ sequence preference for rupturing DNA structure, it generates single strand breaks (SSB) and DSB [12]. BLEO was initially compared to low linear energy transfer (LET) radiations [13], which mainly generate individual DSB, and hence single DNA repair foci well separated one from each other [14]. Nonetheless, BLEO causes also clustered DNA lesions [15, 16], which can comprise clustered DSB among others. These lesions imply the presence of two or more lesions in close proximity [17] and are normally associated to high-LET radiation [18]. In case of clustered DSB DNA repair foci are not necessarily recognizable as individual focus [14]. Due to its genotoxicity, it has been extensively used in chemotherapy for treatment of several types of cancer, such as testicular cancer, certain lymphomas and squamous cell carcinomas.

Conventional fluorescence microscopy is diffraction-limited to ~ 200 nm and ~ 500 nm lateral and axial resolution, respectively, which implies that smaller macromolecular complexes such as DNA repair foci appear blurred and their in-depth organization cannot be unraveled. Under these conditions the visualization of γH2AX foci is restricted to rounded/elliptical nuclear areas of homogeneous intensity, as we noticed in CHO cells when imaging BLEO-induced foci by confocal microscopy [19].

In the last years, a few works have applied what is collectively termed "super-resolution microscopy" or "nanoscopy" to investigate DNA damage repair foci at the nanometer scale. The resolution of such techniques nearly approaches the molecular level (10–100 nm) [20]. By stimulated emission depletion microscopy (STED) Reindl et al. [21, 22] determined that γH2AX and 53BP1 foci, induced either after low- (protons) or high-LET (carbon ions) irradiation in HeLa cells, presented inner nanostructures of round/elongated shape with diameters of ~ 130 nm. Natale et al. [23] arrived at comparable results by combining structured illumination microscopy (SIM) and STED also in HeLa cells but X-ray-exposed. They reported a spatial organization of γH2AX foci in nanoclusters, which in turn, were composed of several smaller structures, referred as nanofoci, with estimated mean diameters of ~ 200 nm (SIM) and ~ 160 nm (STED). Either by immunodetection of phospho-Ku70, which directly associates to broken DNA ends, or using TUNEL assay they concluded that each cluster (rather than nanofoci) corresponded to one DSB.

Among nanoscopies single-molecule localization microscopy (SMLM) provides the highest lateral resolution (~ 20 nm). Indeed, a similar arrangement of circular nanostructures clustered inside γH2AX foci but with a smaller diameter range (Ø = 40–60 nm) was reported by SMLM in a glioblastoma cell line exposed to carbon ions [24]. Based on their size, the authors claimed that these entities, denoted as subfoci elements, may correspond to individual nucleosomes containing γH2AX within DSB repair foci. In agreement, X-ray induced γH2AX in other glioblastoma cell lines were found to be composed of circular nanostructures with a comparable size (Ø ~ 45 nm) [25].

Strikingly, Lopez Perez et al. [24] also reported the presence of isolated nanofoci, outside γH2AX foci but ubiquitously scattered elsewhere in nuclei from control and irradiated cells. A similar distinction between nanofoci, i.e.

clustered in γH2AX foci versus unclustered, was mentioned by Natale et al. [23]. Given the potential implications such isolated all-over γH2AX nanofoci could have in DNA repair dynamics, they deserve further research.

As a new contribution to the field, here we aimed to separately evaluate clustered nanofoci within γH2AX from unclustered nanofoci in control and BLEO-treated HeLa cells imaged by direct stochastic optical reconstruction microscopy (dSTORM), a SMLM technique. A custom cluster analysis method was implemented to individually quantify the two kinds of nanofoci. In addition, to glimpse into their biological characterization, their presence was determined after a deliberate inhibition of the canonical H2AX kinases ATM, ATR and DNA-PK.

Materials and methods

Cell culture

HeLa cells (DSMZ, Germany #161) were routinely cultured in RPMI 1640 with L-glutamine (Sigma-Aldrich R8758) plus 10% (v/v) fetal calf serum (FBS, Sigma-Aldrich F7524), 100 U/mL penicillin 0.1 mg/mL streptomycin (Sigma-Aldrich P4333), 1% MEM non-essential amino acid solution (Sigma-Aldrich F7524), and 1 mM sodium pyruvate (Sigma-Aldrich S8636) in T25-culture flasks at 37 °C and 5% CO_2. Two days before experiments 10.000 cells/well were seeded into 8-well Lab-Tek II chamber slides (Nunc 154534, Thermo Fischer Scientific).

Treatment with bleomycin and H2AX kinase inhibitors

DNA damage was induced by a 45 min BLEO pulse (Sigma-Aldrich 15361) in the absence of FBS. Initially, a dose–response curve (5 to 160 µg/mL BLEO) and a kinetic analysis (allowing 0–2 h recovery in fresh culture medium + FBS after treatment) were carried out. The dose range to test was chosen based on our previous experience with BLEO in CHO cells [19] and other studies which used BLEO to cause genetic damage in HeLa [26, 27]. Then, the 20 µg/mL BLEO dose (BLEO20) without recovery time (0 h) was chosen for later experiments. Controls were carried out by incubation in fresh culture medium (without FBS) during the BLEO pulse.

In order to inhibit ATM, ATR and DNA-PK, HeLa cells were pretreated for 1 h and then co-exposed to BLEO20 plus the inhibitors (one by one and in combinations), namely 20 µM KU-55933 (ATMi, Sigma-Aldrich SML1109) in 0.4% DMSO, 20 µM VE-821 (ATRi, Sigma-Aldrich SML 1415) in 0.4% DMSO and/or 20 µM NU7026 (DNA-PKi, Sigma-Aldrich N1537) in 0.4% DMSO. Vehicle controls were always run in parallel.

γH2AX immunolabeling

Cells were fixed with a 3.7% formaldehyde solution by diluting 1:10 in PBS a 37% formaldehyde stock (Sigma-Aldrich 252549) for 10 min. Then, they were washed in PBS (3 × 5 min), permeabilized (15 min in 0.5% Triton X-100 in PBS), blocked 30 min in 2% BSA in PBS, and then incubated with 1:500 diluted mouse monoclonal anti-γH2AX antibody (Abcam, ab26350) in blocking buffer for 1 h at RT. In addition, controls without primary antibodies (that is, exposed only to blocking buffer) were performed. After washing with 0.1% Tween-20 in PBS (PBS-T, 3 × 5 min), cells were stained for 45 min at RT with secondary antibodies, namely 1:500 Alexa Fluor 532-conjugated goat anti-mouse IgG (Life Technologies A-11002) or 1:500 Alexa Fluor 647-conjugated goat anti-mouse $F(ab')_2$ (Life Technologies A-21237). Finally, cells were washed in PBS-T (3 × 5 min) and kept in PBS for 1 to 5 days, until being imaged by confocal laser scanning microscopy (CLSM) or dSTORM.

Confocal laser scanning microscopy

To evaluate the effect of individual or combined H2AX kinase inhibitors on γH2AX foci formation we used CLSM. Z-stacks of 1024 × 1024 pixels with pixel size 0.198 × 0.198 µm and 1.0 µm step size between optical sections were obtained in a Zeiss LSM 700 microscope (Carl Zeiss GmbH, Jena, Germany) equipped with 555 nm (Alexa Fluor 532) and 639 nm (Alexa Fluor 647) excitation lasers, and a 63 × oil immersion objective (NA = 1.4). Image acquisition settings were kept identical for each experiment to allow comparisons of different treatments. Afterwards, images were analyzed in Fiji software (https://fiji.sc/) to determine the number of γH2AX foci per nucleus in each condition. To do this, we first segmented γH2AX foci by intensity thresholding (constant value per experiment among conditions). Next, the plugin "3D Object Counter" was used to count the total number of foci per stack with a size filter of 5–100 voxels. A maximum volume of 100 voxels was considered to eliminate segmented objects coming from γH2AX pan-nuclear cells. Finally, the number of cells (excluding γH2AX pan-nuclear cells) was determined using the plugin "Cell Counter", which enabled to calculate foci number per nucleus for each condition.

dSTORM imaging

dSTORM relies on the temporal separation of fluorescence emission of individual molecules using dyes which can

undergo reversible photoswitching. To this end, a random read-out of these emissions is attained by transferring the majority of fluorophores to a reversible OFF state and the subsequent stochastic activation and detection of a subset of individual fluorophores. If the probability of activation is low enough, the majority of activated fluorophores residing in their fluorescent ON states are spaced further apart than the diffraction limit and their positions can be precisely determined by a Gaussian fitting of the individual spots. This cycle of photoactivation and read-out is repeated thousands of times allowing the reconstruction of a super-resolution image from all of the single-molecule localizations [28]. Individual cells from controls and cultures exposed to BLEO20, either alone or co-treated with H2AX kinase inhibitors, were imaged by dSTORM. Since suppression of γH2AX foci formation in BLEO20 nuclei was maximized under co-treatment with the pooled 3 kinase inhibitors (ATMi, ATRi, DNA-PKi) (BLEO20 + 3i nuclei) we chose this condition for dSTORM imaging. In addition, to exclude a dose-dependent and/or time-dependent qualitative change in γH2AX foci nanostructure, we imaged cells exposed to BLEO in the 5–160 µg/mL range or allowed to recover post-damage (0.5–2 h) in fresh culture medium.

Immediately before imaging, PBS was replaced by a photoswitching buffer containing 100 mM ß-mercaptoethylamine hydrochloride (MEA, Sigma-Aldrich M6500) in PBS for Alexa Fluor 532, or the same buffer plus an oxygen scavenger system [2% (w/v) glucose, 4 U/mL glucose oxidase and 80 U/mL catalase] for Alexa Fluor 647. In both cases, the buffer pH was set to 7.4 with KOH to achieve an optimal photoswitching effect.

Super-resolution imaging was executed as described previously [28]. In brief, dSTORM images were acquired with an inverted microscope (IX-71; Olympus) equipped with a nosepiece stage (IX2-NPs; Olympus). For excitation of Alexa Fluor 532 and Alexa Fluor 647 a 532-nm diode laser and a 641-nm diode laser (Cube 640-100C, Coherent) spectrally cleaned by a clean-up filter (Laser Clean-up filter 640/10, Chroma) were respectively used.

For each dSTORM measurement we first selected the cell of interest and the focal plane of choice by transmitted light. Then, the fluorescence was turned on and the cell was properly centered at low laser intensities. Next, the irradiation intensity was increased (~ 5 kW/cm^2) to transfer most fluorophores to their off-state. When proper photoblinking was observed (30–60 s later), an image stack of 20,000 frames with an exposure time of 15 ms per frame was recorded in highly inclined and laminated optical sheet (HILO) illumination mode. Super-resolution images were reconstructed in rapidSTORM 3.3 software [29] with a minimum intensity threshold of 600 photons and pixel size of 10 nm.

Cell culture and treatments, immunolabeling as well as CLSM and dSTORM imaging were carried out at the Department of Biotechnology and Biophysics (University of Würzburg, Germany).

Quantitative data analysis

We performed a cluster analysis on localization files generated by rapidSTORM 3.3 with the aim of detecting potential aggregates of γH2AX signal inside nuclei, associated either to γH2AX foci regions or to the remaining nuclear areas. In addition, the nuclear distribution of molecule coordinates among conditions was compared.

For cluster analysis the list of localization coordinates were loaded in the SR-Tesseler software (https://www.iins.u-bordeaux.fr/team-sibarita-SR-Tesseler?lang=en) [30]. SR-Tesseler performs the calculation of 2D Voronoï diagrams (Voronoï tessellation) [31] and allows the subsequent segmentation of groups of localizations as *objects of interest* based on one or more parameters calculated for each localization in the diagram. It has been successfully used with SMLM data from different biological contexts, for instance to decipher the nano-organization of synaptic adhesion proteins in neuron membranes [32], changes in nanocluster density of calcium-handling regulators in mouse myocytes subjected to cardiac hypertrophy [33], the impact of reactive oxygen species on plasma membrane proteins under osmotic stress in *Arabidopsis* [34] or modifications in membrane nanoarrangement of CD4 receptor depending on actin cytoskeleton morphology [35].

The SR-Tesseler software procedure comprises the following steps:

(1) *Voronoï tessellation.* A Voronoï diagram is a set of polygons calculated from the *x*, *y* molecule coordinates in the localization files. Each localization is a point that defines a Voronoï region enclosed by a polygon that has no other nearest localization. The Voronoï polygons are defined from straight segments and segment junction points separating each region from its neighbors: each straight segment is equidistant from two localizations, and the junction points between segments are equidistant from three or more different localizations (exemplified in: https://en.wikipedia.org/wiki/Voronoi_diagram#/media/File:Voronoi_growth_euclidean.gif).

(2) *Parameter-based object-segmentation.* Once the Voronoï polygons are calculated, objects (in our case, clusters of γH2AX signal) are defined as sets of localizations from adjacent Voronoï polygons that have a similar local (first-rank) density and/or lie within a given range of proximity (cut distance). The first-rank density of each localization is calculated considering its neighbor localizations (closer than any other localization), and comparing it against the density of a reference distribution that is spatially uniform, calculated as

the total number of localizations divided by the image area. Next, a *density factor threshold* (α) which is a multiple of the reference localization density is applied to the list of localizations from file: segmented objects of interest are required to have a localization density equal or higher than α. The *cut distance* parameter defines a maximum separation between localizations to consider them as belonging to the same object. A *minimum area* parameter defines a lower threshold value for the area of a given object to be considered.

Segmentation of γH2AX foci regions

We first segmented γH2AX foci regions in control and BLEO20 nuclei in order to separately analyze γH2AX signal inside γH2AX foci from the signal of γH2AX spread elsewhere in the nucleus (Fig. 2). In BLEO20 + 3i cells which exhibited no γH2AX foci this step was not performed. Manual drawings of nuclear contours (regions of interest, ROI) were made for each cell to confine the measurements to nuclear γH2AX signals.

Following the Voronoï tessellation, γH2AX foci were segmented as SR-Tesseler objects on nuclear ROI by adjusting the density factor threshold α and the minimum focus area to be considered. Since an extent of γH2AX focus areas roughly from 0.1 to 0.8 μm^2 has been reported [36], we considered areas greater or equal to 0.025 μm^2 in order to include plausible yet very small foci. The value of α to perform foci segmentation was chosen by trying different values while visually checking the segmentation results (Supplemental Fig. 1). $\alpha = 1.0$ (BLEO20 nuclei) and $\alpha = 2.0$ (controls) produced the best match for the observed γH2AX foci in the original images.

The output of the segmentation step was a text file (named *Export locs ID*), in which each localization was stored and associated to an *object index*. The object index indicated to which focus (object) each localization belonged, with localizations not associated to any focus grouped with index 0. From the *Export locs ID* data of each image, convex hull polygons were calculated for each object by applying a custom Python script (provided as Supplemental Material), in order to generate separate files of (a) localizations within γH2AX foci and (b) remnant, non-foci localizations.

The implemented script defined the following steps:

(1) A convex hull polygon [37] was calculated for each set of localizations with the same object index. In a convex hull polygon, some localizations become polygon vertices, while the rest become interior points. Both were considered as foci localizations. Points located in the exterior of the convex hulls were considered non-foci localizations. It was observed that many localizations from the exterior lied very close to the convex hull polygons but remained outside, which resulted in the appearance of halos surrounding most polygons. The localizations forming the halos belonged to Voronoï polygons significantly larger (low density) that the ones included in the segmentation (high density) and could not be included in γH2AX foci regions without decreasing the optimized α value.
(2) An additional distance parameter d was established to include the localizations composing the halos into segmented γH2AX foci regions within the range specified by this parameter. $d = 50$ nm was found sufficient to remove the halos (Supplemental Fig. 2).
(3) Using the localizations of each convex hull and those within the distance threshold d, a new set of convex hull polygons was calculated. In order to approximate the area of each focus the shoelace algorithm for polygon area [38] was implemented, and applied to the convex hull polygons.
(4) Two localization files were produced as output: one with only γH2AX foci localizations, and the other with the remnant non-foci nuclear localizations.

Quantification of nanofoci confined to γH2AX foci

Localization files containing solely γH2AX foci localizations from control and BLEO20 nuclei were used to identify clusters of γH2AX signal inside them. Nanofoci were segmented by setting $\alpha = 20$, cut distance = 20, and minimum area = 50 nm^2. For each cell, a list comprising the segmented objects along with their individual areas was obtained. Since dSTORM lateral resolution can reach 20–30 nm, and assuming a circular-like shape of nanofoci, objects with areas up to 2000 nm^2 were considered as single nanofoci, between 2000 and 4000 nm^2 as two (partially) fused nanofoci, and so on. Following this rule, the average number and density (number/μm^2) of nanofoci per γH2AX focus in control and BLEO20 nuclei were calculated. Nanofoci areas were estimated as γH2AX foci areas, that is, by setting the additional distance d ($d = 5$ nm) and applying the shoelace algorithm. Then, the area-equivalent diameters assuming a circular-like shape of nanofoci were calculated, according to the formula: $\text{diameter} = \sqrt{4 \cdot \text{area}/\pi}$.

Quantification of scattered γH2AX nanofoci in nuclear regions without γH2AX foci

Localization files from BLEO20 + 3i nuclei and from control or BLEO20 cells comprising the remnant non-foci nuclear localizations were employed to evaluate the presence of scattered γH2AX mark. This signal was segmented by setting $\alpha = 5$, cut distance = 20 and minimum area = 50 nm^2. Calculations were performed as in section above, but considering the nuclear area of remnant non-foci regions in control and

BLEO20 cells to determine nanofoci densities. Their presence was also computed in Ab control images, that is, in cultures incubated only with the secondary antibody.

Statistical analysis

Two-sample unpaired *t*-test and one-way ANOVA with Bonferroni correction were performed when necessary, with a 95% confidence level.

Results

BLEO-induced γH2AX foci: dose–response curve, foci kinetics and sensitivity to ATM, ATR and DNA-PK kinase inhibitors

To select an appropriate working condition to perform a complete dSTORM image analysis in HeLa cells, preliminary experiments were carried out varying BLEO exposure dose (range 5–160 μg/mL) and post-damage recovery time (0–2 h). The dose–response curve showed a steady level of γH2AX foci number between 5 and 80 μg/mL BLEO, with an increase after 160 μg/mL BLEO exposure (Supplemental Fig. 3a). To our purpose, we considered that BLEO20 was enough to induce a robust foci number increase, tripling those found in control cells. Early kinetics (0–2 h post-treatment) showed no increase in foci number as recovery time extended (Supplemental Fig. 3b). For this reason, the easiest experimental scheme was chosen, namely fixing the cells immediately after the 45 min treatment.

The γH2AX signal specificity was tested by employing inhibitors of H2AX kinases (ATM, ATR and DNA-PK), with the aim of suppressing the phosphorylation of H2AX to γH2AX after BLEO insult. As shown in Supplemental Fig. 4a, γH2AX foci formation was mainly dependent on ATM. In contrast, ATR and/or DNA-PK inhibition displayed no effect by their own. Instead, their effect was evident only if ATM was also inhibited. The fact that foci were primarily ATM-dependent suggests that they had originated from DNA DSB rather than from collapsed/stalled replication forks (which would have implied an ATR-dependent H2AX phosphorylation). The preferential involvement of ATM over DNA-PK in response to DSB is in agreement with Burma et al. [39]. Since the simultaneous use of the three inhibitors dropped foci number to control levels we chose this combination to perform dSTORM imaging.

Pan-nuclear γH2AX signal was not abrogated by the pooled ATM/ATR/DNA-PK kinase inhibitors

It is worth to mention that, now and then, γH2AX pan-nuclear cells were observed in all BLEO-treated cultures, even under the simultaneous treatment with the three kinase inhibitors (Supplemental Fig. 4b–i). Conversely, they were completely absent in control and DMSO-treated cells (Supplemental Fig. 4j). A nuclear-wide γH2AX formation, involving the entire chromatin, has been proved to be involved in apoptosis, for example by exposure to TNF-related apoptosis-inducing ligand (TRAIL) [40], BLEO [19] and UV irradiation of DNA-replicating cells [41]. In addition, a fainter γH2AX pan-nuclear staining unrelated to apoptosis but dependent on DNA damage level has been described specifically in G1/G2 cells after exposure to heavy ions [42]. As we suggested in CHO cells [19], an apoptotic process due to BLEO treatment could have been triggered above a certain critical amount of DNA damage. Alternatively, it has been reported that BLEO can trigger apoptosis in a DNA damage-independent extrinsic pathway, dependent on caspase-8 [43].

The pan-nuclear H2AX phosphorylation has been described to be regulated by another set of kinases (and not ATM, ATR and DNA-PK). They include Mst-1 in the JNK1/caspase-3 dependent cell death [44] and a distinct p38 mitogen-activated protein kinase (MAPK) pro-apoptotic pathway [45] which, as expected, were not affected by the specific inhibitors we used to abate ATM, ATR and DNA-PK. A further analysis of this phenomenon was out of the scope of the present work.

Both endogenous and BLEO-induced γH2AX foci were organized in nanometric substructures

Next, the structure of γH2AX foci at nanometer scale by dSTORM was investigated. In cultures exposed to BLEO20 we observed clumps of γH2AX signal (i.e. nanofoci) as substructures of the γH2AX foci observed by standard fluorescence microscopy (Fig. 1b, f, j). The fewer endogenous γH2AX foci in control cells exhibited a similar nanometric organization (Fig. 1a, e, i). In addition, no substantial modifications in γH2AX foci sub-organization were appreciated either with different doses (Supplemental Fig. 3c–f) or post-damage recovery times (Supplemental Fig. 3g–j). To check the reliability of dSTORM results, we used a different secondary antibody to detect γH2AX, which yielded a similar outcome (Supplemental Fig. 3l). As shown on Fig. 1c, BLEO-induced foci completely disappeared from dSTORM-reconstructed images when cells were simultaneously exposed to the three inhibitors (BLEO20 + 3i nuclei).

Nuclear segmentation according to γH2AX status: on average BLEO-induced foci area was larger (~ 2 times) than endogenous foci area of control cells

Besides the nanometric signal within γH2AX foci, we detected in all cases a γH2AX mark scattered throughout the

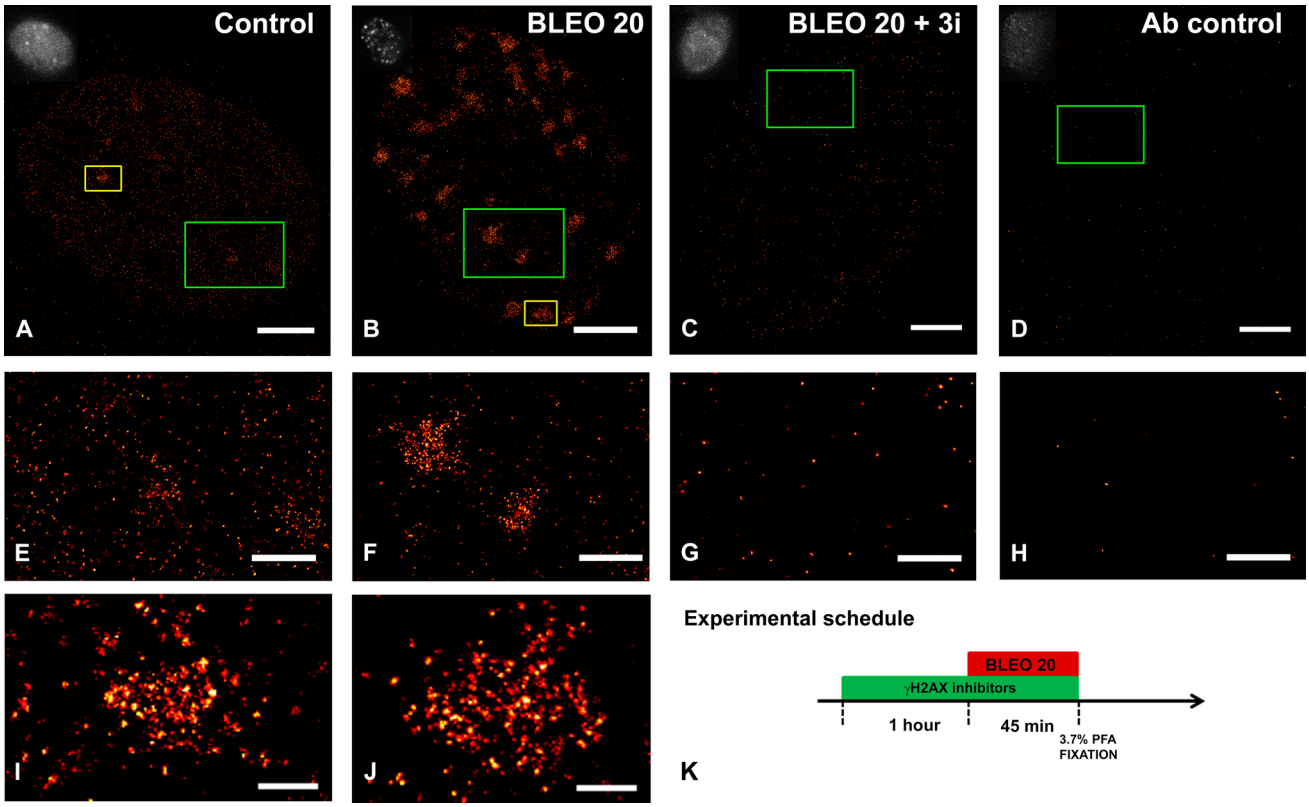

Fig. 1 Control and BLEO-induced γH2AX foci are composed of smaller nanometric substructures (nanofoci) as revealed by dSTORM super-resolution imaging. HeLa cells were untreated (**a**) or exposed to 20 µg/mL BLEO (BLEO20) for 45 min alone (**b**, **d**) or with (**c**) a pre- (1 h) and co-treatment with pooled kinase inhibitors (i), namely KU-55933 (ATMi), VE-821 (ATRi) and NU7026 (DNA-PKi) (20 µM each). Then, cells were fixed in 3.7% PFA and indirectly immunolabeled with a primary mouse anti-γH2AX (Abcam, ab26350) antibody and a secondary Alexa Fluor 647-conjugated anti-mouse antibody (**a**–**c**) or exposed only to the secondary antibody (**d**). **a**–**d** Whole nuclear images reconstructed in rapidSTORM 3.3. Bar: 3 µm. Upper left insets: corresponding γH2AX images for each nucleus by standard wide-field fluorescence microscopy. **e**–**h** Enlarged views (large green boxes) from **a**–**d**. Bar: 1 µm. **i** and **j** Enlarged views (small yellow boxes) from **a**, **b**. Bar: 300 nm. γH2AX foci either from control or BLEO-treated nuclei were organized in nanoscopic substructures (**a**, **b**, **i**, **j**). BLEO-induced foci vanished when cells were exposed to H2AX kinase inhibitors (compare **b** to **c**). Besides, cells incubated with the γH2AX primary antibody exhibited a dotted γH2AX signal scattered throughout the nucleus (compare signals in **e**–**g** with signal in **h**). As expected, no signal was observed when immunolabeling was performed in absence of primary antibodies (**d**, **h**). **k** Experimental schedule. HeLa cells were pretreated for 1 h with 20 µM of ATM, ATR and DNA-PK inhibitors and then co-exposed for 45 min to BLEO20 and the inhibitors before being fixed in 3.7% PFA. (Color figure online)

nucleus as long as cells were incubated with the anti-γH2AX primary antibody (compare signals in Fig. 1e–g versus h).

To separately analyze the clustered γH2AX signal inside γH2AX foci (clustered nanofoci) and the scattered signal from the remnant nuclear areas, we first generated two images from each original localization file of control and BLEO20 nuclei by combining SR-Tesseler segmentation and a custom Python script based on the convex hull of the foci regions (see workflow on Fig. 2, and "Materials and methods" section). Even though we could successfully segment the areas of γH2AX foci from the rest of the nucleus in SR-Tesseler (Fig. 2c), a halo of localizations surrounding each extracted focus persisted in the images devoid of foci (Fig. 2d). To address this issue, we extended the set of localizations to be extracted from these images (50 nm of additional distance from the boundary of each convex hull) to incorporate them to their respective foci. The result was sets of pictures of control and BLEO20 nuclei having exclusively regions of γH2AX foci (Fig. 2e) or the complementary non-foci areas (Fig. 2f).

As a result of the described processing, mean foci areas of 0.41 μm^2 (BLEO20) and 0.19 μm^2 (controls) were obtained. BLEO-induced foci presented a higher heterogeneity in size than endogenous foci, which mostly exhibited areas $\leq 0.3\ \mu m^2$ (~ 88% from total number) (Supplemental Fig. 5). In BLEO20 nuclei a foci subpopulation (7.5%) presented areas $> 1\ \mu m^2$. A proportion of them could correspond to two foci partially overlapped, which could not be separated one from each other through the segmentation. Mean values are in line with previous reports [36,

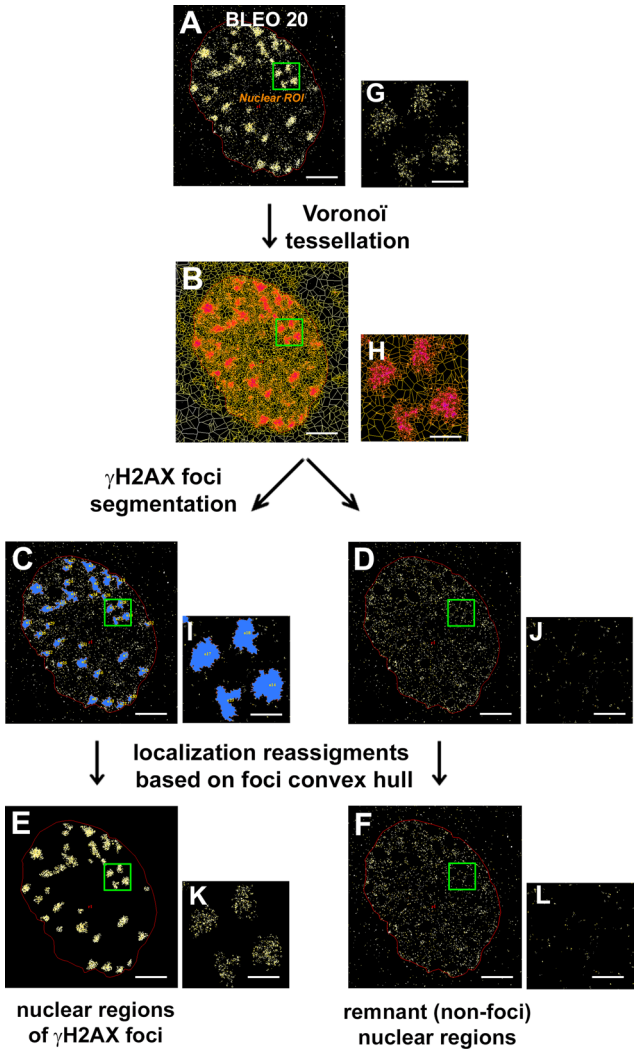

Fig. 2 Image segmentation of BLEO20 and control nuclei into (i) regions harboring γH2AX foci and (ii) remnant (non-foci) regions. SR-Tesseler software was used to define the foci regions, and a custom Python script was implemented to filter out localizations based on the convex hull of the foci regions (see "Materials and methods" section). **a**–**f** Steps carried out to obtain two separate images from each original picture are exemplified in a BLEO20 nucleus. **a** Image from localizations file, **b** Voronoï tessellation, and **c** subsequent segmentation of γH2AX foci regions (blue) from the entire nucleus in SR-Tesseler by setting $\alpha = 1$ and minimum area = 0.025 μm^2. **d** Resulting image with localizations belonging to γH2AX foci (**c**) subtracted from image (**a**). A halo of points (localizations) surrounding each substracted γH2AX focus remained in the picture. To correct this, a convex hull was computed for each focus, with an additional border distance of 50 nm to filter out an extended set of localizations. With this procedure, the localizations belonging to halos were removed from (**d**) and reassigned to (**e**). The final result was a set of images only with γH2AX foci regions (**e**) or the remnant non-foci nuclear regions (**f**). The nuclear ROI (r_1) is outlined by the red line. Bar: 3 μm. **g**–**l** Enlarged (×4) views (green boxes) from images **a**–**f**, respectively. Bar: 750 nm. (Color figure online)

46], which supports the approach of a refined foci segmentation by combining SR-Tesseler with a neighborhood distance parameter to include localizations from object surroundings.

BLEO-induced γH2AX foci contained as average almost double nanofoci than endogenous control foci

Images of control and BLEO20 nuclei harboring only the segmented regions of γH2AX foci (Fig. 3a, e) were used to quantify γH2AX nanofoci inside each γH2AX focus. A segmentation by SR-Tesseler in this set of images was implemented (Fig. 3b, f) to identify such smaller nuclear clusters in the context of a much bigger microscopic γH2AX focus. Since in this case the localizations exhibited a spotted nuclear pattern of small and dense clusters, a high density factor threshold ($\alpha = 20$) was needed to achieve a satisfactory nanofoci segmentation. Zoomed images (Fig. 3c, d, g, h) revealed that each focus was formed by individual nanofoci in a variable number.

Among individual control (Fig. 3j) or BLEO20 nuclei (Fig. 3k) the number of nanofoci per focus was independent from foci number per cell. The bigger γH2AX foci in BLEO20 nuclei exhibited a similar density of nanofoci per focus than the endogenous foci in controls, and thus more nanofoci per focus (mean 22.7 in treated cells versus 13.2 in controls; Fig. 3l, m).

Nucleoplasm of control and BLEO-treated cells harbored scattered nanofoci outside γH2AX foci, which were partially sensitive to kinase inhibitors

As previously mentioned, apart from nanofoci confined to γH2AX foci in all conditions unclustered γH2AX nanofoci spread throughout the nucleus were noticed. We selected the set of pictures comprising non-foci regions from control (Fig. 4a) and BLEO20 nuclei (Fig. 4b), the images corresponding to BLEO20 + 3i (inherently without γH2AX foci) (Fig. 4c) and Ab control cells (Fig. 4d), and computed their average nanofoci number and density after SR-Tesseler segmentation.

A significant contribution of the secondary antibody to the γH2AX signal was discarded since the amount of mark in Ab control cells was negligible (Fig. 4i). Control and BLEO20 nuclei exhibited similar densities of scattered γH2AX nanofoci per nuclear section (~ 3 nanofoci/μm^2), suggesting that they originated endogenously (unrelated to BLEO-induced DNA damage). In favor of the specificity of the signal, BLEO20 + 3i cells exhibited a 50% diminution of signal density when contrasted to cells exposed only to BLEO20. The estimated mean nanofoci diameter (~ 50 nm) was conserved among clustered and unclustered nanofoci in all conditions (Fig. 4m).

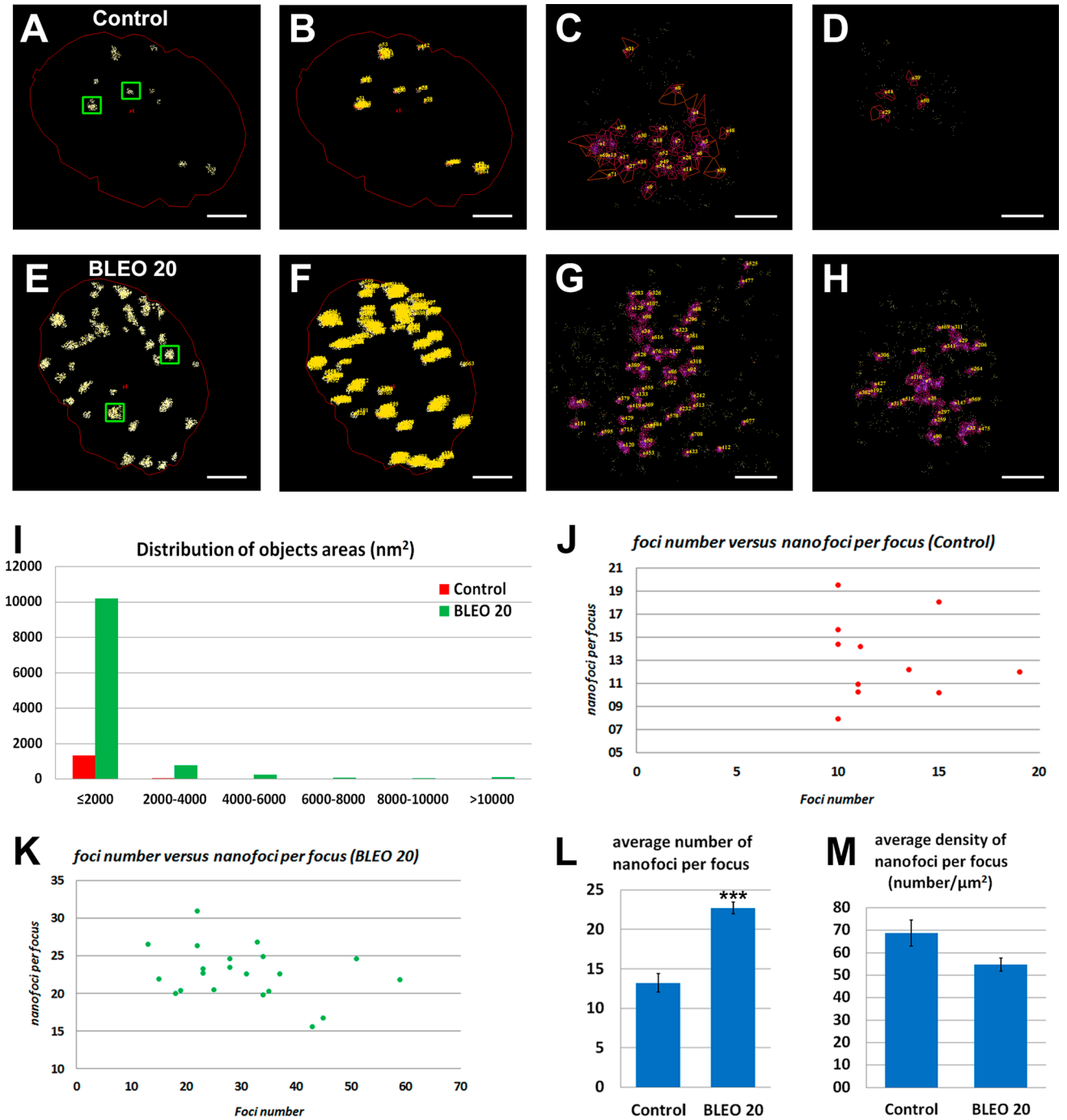

Fig. 3 Quantification of nanofoci confined to γH2AX foci regions by SR-Tesseler. **a**–**d** Control and **e**–**h** BLEO20 nuclei images are shown. **a**, **e** Images of nuclei harboring only the segmented γH2AX foci regions (Fig. 2). Nuclear ROI (r_1) are outlined by red lines. **b**, **f** Segmentation in SR-Tesseler of γH2AX nanofoci from **a**, **e** by setting $\alpha=20$, cut distance=20 and minimum area=50 nm^2. **a**, **b**, **e**, **f** Bar: 3 µm. **c**, **d**, **g**, **h** Enlarged views (×16) from green boxes indicated in **a** and **e**, respectively. Bar: 200 nm. Zoomed images show that each γH2AX focus is formed by individual nanofoci in a variable number. **i**–**m** Altogether, $n=1392$ (control) and $n=11{,}471$ (BLEO20) segmented objects coming from $n=11$ (control) and $n=21$ (BLEO20) cells were analyzed (data from three independent experiments). **i** Histogram displaying the distribution of object areas (nm^2) for control and BLEO20 nuclei. As discussed before (see "Materials and methods" section) segmented objects with areas between 50 and 2000 nm^2 were considered as single nanofoci, between 2000 and 4000 nm^2 as two (partially) fused nanofoci, and so on. As depicted in the histogram, most objects were single nanofoci in both cases (95% and 89% for BLEO20 and control nuclei, respectively). **j** and **k** Plots of foci number versus number of nanofoci per focus for each analyzed control (**j**) and BLEO20 (**k**) nucleus. As seen in the plots, no apparent correlation between these variables was observed either for control or BLEO20 nuclei (linear correlation coefficient values $r=0.0052$ and 0.0042, respectively). **l** Number and **m** density (number/µm^2) of nanofoci per γH2AX focus (mean ± standard error) for control and BLEO20 nuclei. Although a higher mean number of nanofoci per focus was detected in BLEO20 compared to controls (22.7 versus 13.2; ***$p<0.001$; two-sample unpaired *t*-test), comparable average densities were found due to smaller mean areas of foci in controls. (Color figure online)

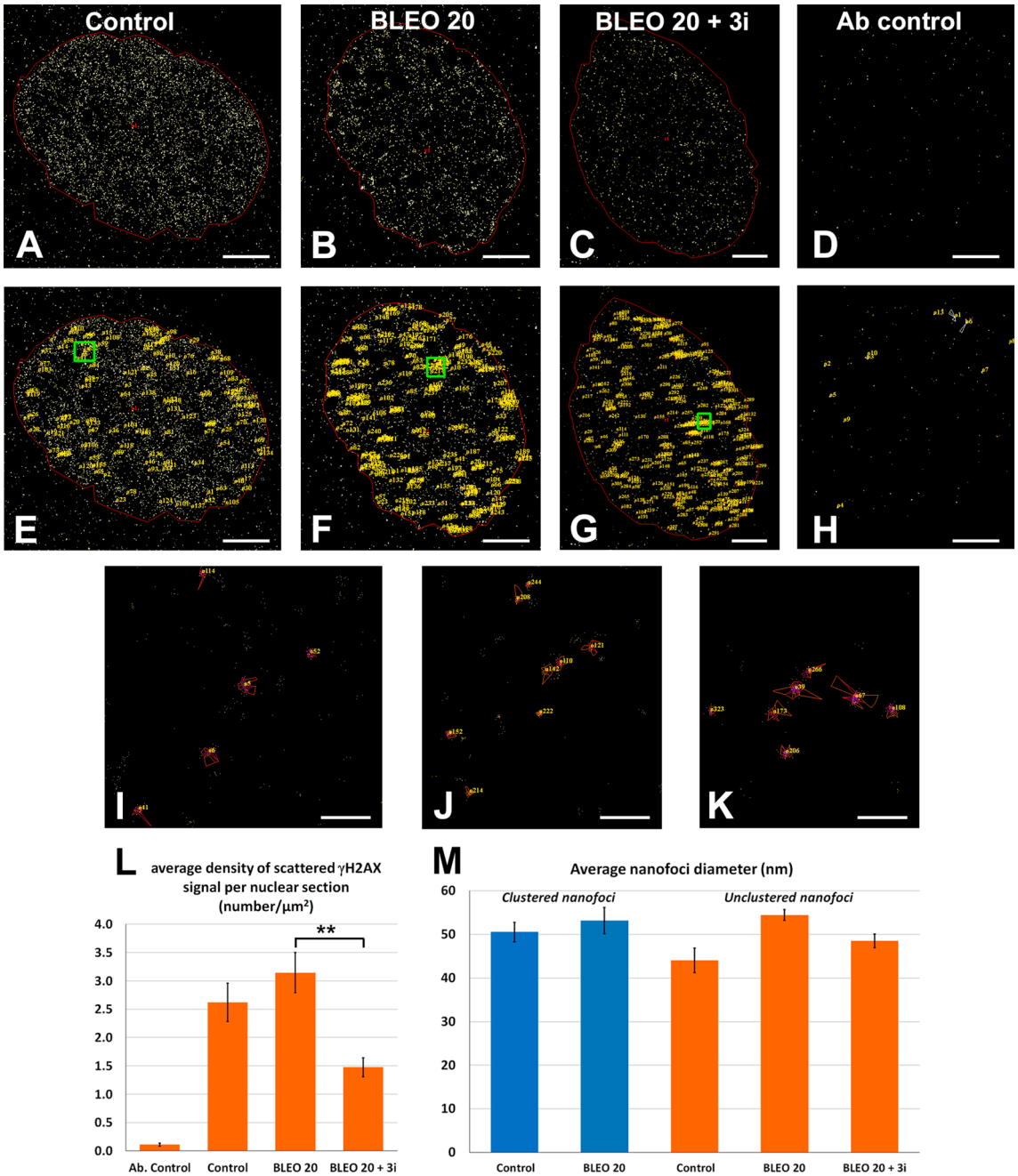

Fig. 4 Quantification of unclustered nanofoci in nuclear regions devoid of γH2AX foci by SR-Tesseler. **a**, **e**, **i** Control, **b**, **f**, **j** BLEO20, **c**, **g**, **k** BLEO20 + 3i and **d**, **h** Ab control images are shown. **a** and **b** Images of nuclei with remnant (non-foci) regions from control and BLEO20 (Fig. 2). **c** and **d** images from the localization file of a BLEO20 + 3i and Ab control nuclei in SR-Tesseler. **e**–**h** Segmentation of scattered γH2AX signal from **a**–**d** in SR-Tesseler by setting $\alpha = 5$, cut distance = 20 and minimum area = 50 nm^2. **a**–**h** Bar: 3 μm. Nuclear ROI (r_1) are outlined by the red lines. **i**–**k** Enlarged views (×16) from green boxes indicated in **e**–**g**, respectively. Bar: 200 nm. **l** Density (number/μm^2) of scattered γH2AX signal per nuclear section (mean ± standard error) for control, BLEO20 and BLEO20 + 3i ($n = 11$) cells. In total, $n = 3405$ (control), $n = 8060$ (BLEO20) and $n = 2998$ segmented objects were analyzed. Since nuclear ROI cannot be precisely defined in Ab control ($n = 8$) the average density for the whole image was considered (data from three independent experiments). A similar density of scattered γH2AX signal per nuclear section was found between control and BLEO20 nuclei. Conversely, BLEO20 + 3i cells exhibited a lower average density in comparison to cells exposed to BLEO20 (**$p < 0.01$; one-way ANOVA with Bonferroni correction). Signal density in Ab control was negligible when contrasted to the samples incubated with the primary anti-γH2AX antibody. **m** Estimated diameters (nm) of clustered (blue columns) and unclustered (orange columns) nanofoci (mean ± standard error) for control, BLEO20 and BLEO20 + 3i nuclei. First, nanofoci areas were calculated as γH2AX foci areas, i.e. setting the parameter d and then applying the shoelace algorithm. Then, diameters were computed considering a circular-like shape of nanofoci. Estimated mean values ranged among ~ 44 nm (control, unclustered) and ~ 54 nm (BLEO20, unclustered). Nevertheless, differences in nanofoci diameters were not significant, neither among conditions ($p \geq 0.16$) nor when clustered nanofoci were compared against unclustered nanofoci within a given treatment ($p \geq 0.14$). (Color figure online)

Discussion

In the present work, we have demonstrated in HeLa cells that BLEO20-induced γH2AX foci are organized as clusters of nanofoci. Compared to endogenous foci, the more abundant BLEO-induced foci are qualitatively similar (even using high BLEO doses, up to 160 µg/mL) but quantitatively different, since they approximately duplicate endogenous foci in size and internal nanofoci number.

Endogenous γH2AX foci are ascribed to DSB produced at stalled and collapsed replication forks [7], linked to alterations in the progression of the transcriptional machinery or the collision between the replication and the transcriptional complexes [8], and originated in nuclear regions implicated in 3D genome organization [9]. As already reported in various cell lines (including HeLa) and primary cultures endogenous γH2AX foci present, on average, tinier mean sizes compared to DNA damage-associated foci [36, 46, 47]. By our novel segmentation approach, comparable results were obtained since DSB-related foci were twice bigger than endogenous foci in controls. In the case of BLEO-induced foci, a similar level of foci number was obtained in the 5–80 µg/mL range, with an increase only after exposure to BLEO 160 µg/mL. Previous results with the radiomimetic in CHO cells already had shown a non-linear relationship among foci number and BLEO doses [19]. Several factors could contribute to this overall result, namely the need for membrane transporters to enable the access of BLEO to the cells [48], a putative participation of the enzyme BLEO hydrolase, which could provide resistance to BLEO [49], and a differential cell sensitivity to the agent according to cell cycle phase (G1/G2 are more damage-prone than S cells) [50]. In addition, BLEO requires the presence of cofactors, oxygen and the reduced transition metals Fe(II) or Cu(I) [12, 51], to become the activated form capable of inducing DSB. In fact, it has been shown by Comet assay that BLEO produces a heterogeneous level of DNA-damage in HeLa cells, highly variable from cell to cell, when compared to IR-induced damage [52]. In short, a larger number of nuclei per experimental condition should have been evaluated, had it been our objective to study BLEO dose–response in HeLa cells.

By dSTORM we confirmed in BLEO-treated cells other recent works which, thanks to the cutting-edge increase in resolution provided by nanoscopy, demonstrated that γH2AX foci observed by conventional fluorescence microscopy own an internal organization consisting of smaller sub-structures (i.e. nanofoci). Individual bunches of clustered nanofoci have been argued to be the basic unit for DSB repair [23, 24]. As suggested by Lopez Perez et al. [24], individual nanofoci may indicate single nucleosomes harboring γH2AX, while their arrangement as clusters would represent the local chromatin structure required for DSB DNA repairing. In fact, each individual nanofocus corresponds to a chromatin loop, which is disposed into a higher-order structure of discontinuously phosphorylated chromatin, with a size comparable to that of clustered nanofoci [23]. The nanodomains are flanked by CTCF (CCCTC-binding factor), a transcriptional repressor implicated in the regulation of chromatin architecture [53].

We determined, on average, 13.2 and 22.7 nanofoci per focus in control and BLEO20 nuclei respectively, which entailed a comparable mean density per focus (~60 nanofoci/µm^2 per nuclear section) in both conditions. Sisario et al. [25] reported ~16 and ~20 nanofoci per focus in control and X-ray-irradiated glioblastoma cells, respectively. In addition, comparable diameters of clustered nanofoci were determined when estimated by our analysis approach (~52 nm versus ~45 nm in [25]). Moreover, Lopez Perez et al. [24] compared clustered versus scattered nanofoci diameters, reporting a larger diameter (~25% increment) of clustered nanofoci both in controls and radiation-treated nuclei. We could not detect such a difference in our study. All things considered, even though image analysis methods varied among studies the quantitative results are strikingly close, pointing out to consistent results by SMLM.

Apart from clustered nanofoci confined to γH2AX foci we also detected scattered nanofoci in the remnant nucleoplasm, both in control and BLEO20 cells. To our knowledge, the presence of such an all-over scattered nuclear signal has been solely studied by Lopez Perez et al. [24]. By carbon-ion irradiation they found an increment in the number of nanofoci not associated to foci regions (i.e. out of ion tracks). In our case, the scattered signal was analyzed separately by a novel custom methodology (summarized in Fig. 2). We concluded that unclustered γH2AX nanofoci were equally present at low density, both in control and BLEO20 nuclei (~3 nanofoci/µm^2). This finding would suggest an endogenous level of H2AX phosphorylation independent of DNA damage induction. Lopez Perez et al. [24] hypothesized that, albeit arguable, the increase from the endogenous level they determined could be attributed to isolated DSB induced by an indirect-derived radiation expanding from the ion tracks. In addition, they proposed the previously reported faint γH2AX pan-nuclear staining due to ion irradiation [42], as a possible cause of nanofoci increment. In any case, such an effects are not expected on BLEO-treated cells, and hence to impact in the levels of scattered nanofoci.

A basal level of γH2AX signal could respond to transient DSB, formed during endogenous DNA metabolism, which do not trigger an active DNA damage response (that is, microscopic γH2AX foci induction). Unclustered nanofoci could, hence, represent a starting point of scarce local H2AX

phosphorylation on DNA for putative DSB repair units. Some hints in this line have been given employing methods of genome-wide DSB profiling. Thus, an enrichment of endogenous γH2AX at loci susceptible to replication fork stalling and breakage has been found in yeast using ChIP-chip data [54]. Similarly, genome-wide localization sites of H2AX and γH2AX, either endogenous or IR-induced, have been mapped in proliferating and resting human cells [55]. In replicating cells, endogenous γH2AX-enriched regions covered sub-telomeres and active transcription start sites (TSS). In fact, H2AX itself, prior to phosphorylation, was specifically located in these spots. On the contrary, in resting cells an endogenous γH2AX signal was not detectable. Cellular demand for DNA repair correlates with the potential to replicate, and hence, as proven [56], it is globally attenuated in terminally differentiated cells. Tumor cells undergo much more cell division cycles, and thus present a higher demand of response to DNA damage. So, endogenous γH2AX-enriched regions in dividing cells could be indicating replication- and transcription-mediated stress due to their rapid cell division cycles. The pattern of well-distributed scattered γH2AX nanofoci detected in HeLa, a tumor-derived cell line, could reflect a required level of endogenous γH2AX in order to provide protection against a potential high level of transient DSB. Interestingly, Seo et al. [55] verified a spread from the active TSS into the gene body after irradiation, a process compatible with the later emergence of microscopic γH2AX foci. Finally, it cannot be discarded that unclustered nanofoci indicate either another type of DNA lesion (and not DSB) or even a distinct γH2AX role, unlinked to DDR, as those already reviewed [57].

Here, as a novel contribution, we evaluated by SMLM (dSTORM) the occurrence of γH2AX nanofoci in cells challenged with specific inhibitors of canonical H2AX kinases (i.e. ATM, ATR and DNA-PK). Although recent works have studied γH2AX nanofoci in a very comprehensive way [21–25, 58], to our knowledge this is the first time in which nanofoci were investigated after a deliberate attempt to inhibit H2AX phosphorylation. In this regard, we could confirm the specificity of the γH2AX mark reconstructed from SMLM data since BLEO-induced foci completely disappeared from dSTORM images when cells were simultaneously exposed to ATM, ATR and DNA-PK inhibitors. This finding was as expected, since it fits the positive activation loop of H2AX kinases [59]. In turn, under these conditions, the γH2AX scattered mark did not completely fade out but diminished in nuclear density (~50%). This might respond to several, non-exclusive factors. First, although the concentrations (20 μM) of KU-55933, VE-821 and NU7026 that we used to inhibit ATM, ATR and DNA-PK were well above their IC_{50} values (12.9 nM, 13 nM and 230 nM in cell-free assays, respectively), and no foci were detected in their presence, it cannot be discarded that the 1 h pretreatment was not enough to achieve a complete inhibition of the target kinases, or that the half-life of pre-existent scattered nanofoci was longer than 1 h. We assayed a longer pretreatment with the pooled inhibitors (24 h) before BLEO-exposure but it resulted in a significant cytotoxicity, revealed by a very low cellular density and a considerable proportion (~75%) of (apoptotic) pan-nuclear γH2AX cells (data not shown). Second, the action of other kinases able to phosphorylate H2AX at Ser139 could explain the remnant γH2AX signal. While the activation of MAPK family members p38 and Mst-1 has been reported only in apoptotic contexts [44, 45], a newly described chromatin kinase-termed VRK1 has been proved to phosphorylate H2AX to γH2AX in response to DNA damage induced by γ-rays [60]. Importantly, even in basal conditions VRK1 directly interacts with H2AX, which raises the possibility of a specific VRK1 role in endogenous H2AX phosphorylation. In addition, VRK1 impact on H2AX was unaffected by KU-55933 and caffeine (a general PI3K inhibitor). In the same line, if scattered nanofoci allude to DNA lesions aside from DSB, unknown H2AX kinases might play a role in their phosphorylation. Third, a nonspecific labeling of γH2AX primary antibody to other nuclear structures apart from γH2AX cannot be formally discarded, although it seems very unlikely since unclustered nanofoci have been observed by others [23, 24]. Last but not least, while γH2AX can be dephosphorylated in situ by PP2A [61] and PP4 [62], a significant fraction of γH2AX could be released from chromatin by exchange with unphosphorylated H2AX, as revealed by fluorescence recovery after photobleaching (FRAP) experiments using GFP-H2AX [63]. Thereby, γH2AX dephosphorylation can also occur in the nucleoplasm, far away from the corresponding DSB lesion site. In this context, the residual γH2AX signal could point out to persistent γH2AX already dissociated from damaged chromatin.

It is worth mentioning that in all conditions we observed the presence of γH2AX signals outside the nuclear region, presumably in cytoplasmic areas (Supplemental Fig. 6). To date, the appearance of γH2AX in the cytoplasm has been only described in association to tropomyosin-related kinase A (TrkA)/JNK1-induced cell death in U2OS cells independently from DNA damage induction [64]. Since external cytoplasm boundaries could not be precisely defined in the images, we were not able to calculate and compare signal densities between experimental conditions. Further research would be needed to find out whether the cytoplasmic signal we detected does correspond or not to cytoplasmic γH2AX.

In conclusion, untreated HeLa cells harbored scattered γH2AX nanofoci as well as clustered nanofoci confined to a few microscopic γH2AX foci. After exposure to BLEO, γH2AX foci increased in number and size but

their nano-organization was comparable to those found in untreated cells. The level of scattered γH2AX nanofoci remained unchanged, pointing to an endogenous generation. A pool of specific H2AX kinase inhibitors erased BLEO-induced clustered nanofoci but only partially the endogenous scattered nanofoci, which opens the door to consider the putative role of a recently described H2AX kinase (VRK1) in the formation of γH2AX nanofoci.

In recent years, super-resolution microscopy has revealed previously undisclosed protein distribution patterns and nanostructural features, not detectable by conventional microscopy. Of note, these new findings ask for consistent analytical tools to process and analyze signals at the nanoscale level. Here, we provide a novel approach to address cluster analysis from SMLM data. It could be particularly useful when dealing with clusters of very dissimilar densities, such as scattered nanofoci coexisting with clustered nanofoci organized in microscopic foci.

Acknowledgements We wish to express our gratitude to Markus Sauer for the invitation to perform dSTORM experiments at the Department of Biotechnology and Biophysics (University of Würzburg) as well as to Pablo Mateos-Gil, Sebastian Letschert and Fabian Zwettler for training and advice in dSTORM methodology (PL). We are also indebted to ANII (National Agency for Research and Innovation, Uruguay) for PhD Scholarship (POS_NAC_2014_1_102214) to PL as well as research support to LL-H and GF, and to PEDECIBA (Program for the Development of Basic Sciences, Uruguay). Research in SCIAN-Lab is funded by the Chilean Millennium Scientific Initiative P09-015-F to IC, JJ-W, SH; FONDECYT 11170475 to IC; FONDECYT 1181823 to IC, SH; FONDECYT 1161274, FONDECYT Ring Initiative ACT-1402, DAAD 57220037 and 57168868, CORFO 16CTTS-66390 to SH; CONICYT PhD Scholarship to JJ-W.

Author contributions PL: conceived and designed studies, performed research, analyzed data and wrote the draft manuscript. JJ-W co-wrote data analysis section in Materials and Methods and revised the manuscript. JJ-W, IC and SH developed the scripts for processing the SR-Tesseler files and contributed to data analysis. LL-H: contributed to design experiments, data interpretation and revised the manuscript. GF: revised the manuscript.

Compliance with ethical standards

Conflict of interest The authors declare that they have no conflict of interest.

References

1. Rogakou E, Pilch D, Orr A, Ivanova V, Bonner W (1998) DNA double-stranded breaks induce histone H2AX phosphorylation on serine 139. J Biol Chem 273:5858–5868
2. Ward I, Chen J (2001) Histone H2AX is phosphorylated in an ATR-dependent manner in response to replicational stress. J Biol Chem 276:47759–44762
3. Kinner A, Wu W, Staudt C, Lliakis G (2008) γH2AX in recognition and signaling of DNA double-strand breaks in the context of chromatin. Nucleic Acids Res 36:5678–5694
4. Rogakou E, Boon C, Redon C, Bonner W (1999) Megabase chromatin domains involved in DNA double-strand breaks *in vivo*. J Cell Biol 146:905–915
5. Celeste A, Difilippantonio S, Difilippantonio M, Fernandez-Capetillo O, Pilch D, Sedelnikova O, Eckhaus M, Ried T, Bonner W, Nussenzweig A (2003) Histone H2AX phosphorylation is dispensable for the initial recognition of DNA breaks. Nat Cell Biol 5:675–679
6. Jackson SP, Bartek J (2009) The DNA-damage response in human biology and disease. Nature 461:1071–1078
7. Gelot C, Magdalou I, Lopez BS (2015) Replication stress in mammalian cells and its consequences for mitosis. Genes 6:267–298
8. Vitelli V, Galbiati A, Iannelli F, Pessina F, Sharma S, d'Adda di Fagagna F (2017) Recent advancements in DNA damage-transcription crosstalk and high-resolution mapping of DNA Breaks. Annu Rev Genomics Hum Genet 18:87–113
9. Bouwman B, Crosetto N (2018) Endogenous DNA double-strand breaks during DNA transactions: emerging insights and methods for genome-wide profiling. Genes (Basel) 9:E632
10. Chen HT, Bhandoola A, Difilippantonio MJ, Zhu J, Brown MJ, Tai X, Rogakou EP, Brotz TM, Bonner WM, Ried T, Nussenzweig A (2000) Response to RAG-mediated V(D)J cleavage by NBS1 and γ-H2AX. Science 290:1962–1965
11. Umezawa H, Maeda K, Takeuchi T, Okami Y (1966) New antibiotics, bleomycin A and B. J Antibiot (Tokyo) 19:200–209
12. Chen J, Stubbe J (2005) Bleomycins: toward better therapeutics. Nat Rev Cancer 5:102–112
13. Henner WD, Grunberg SM, Haseltine WA (1982) Sites and structure of gamma radiation-induced DNA strand breaks. J Biol Chem 257:11750–11754
14. Oike T, Niimi A, Okonogi N, Murata K, Matsumura A, Noda SE, Kobayashi D, Iwanaga M, Tsuchida K, Kanai T, Ohno T, Shibata A, Nakano T (2016) Visualization of complex DNA double-strand breaks in a tumor treated with carbon ion radiotherapy. Sci Rep 6:22275
15. Regulus P, Duroux B, Bayle PA, Favier A, Cadet J, Ravanat JL (2007) Oxidation of the sugar moiety of DNA by ionizing radiation or bleomycin could induce the formation of a cluster DNA lesion. Proc Natl Acad Sci USA 104:14032–14037
16. Mavragani IV, Nikitaki Z, Souli MP, Aziz A, Nowsheen S, Aziz K, Rogakou E, Georgakilas AG (2017) Complex DNA damage: a route to radiation-induced genomic instability and carcinogenesis. Cancers (Basel) 9:91. https://doi.org/10.3390/cancers9070091
17. Schipler A, Iliakis G (2013) DNA double-strand-break complexity levels and their possible contributions to the probability for error-prone processing and repair pathway choice. Nucleic Acids Res 41:7589–7605
18. Nickoloff JA, Sharma N, Taylor L (2020) Clustered DNA double-strand breaks: biological effects and relevance to cancer radiotherapy. Genes (Basel) 11(1):99
19. Liddle P, Lafon-Hughes L, Di Tomaso MV, Reyes-Ábalos AL, Jara J, Cerda M, Härtel S, Folle GA (2014) Bleomycin-induced γH2AX foci map preferentially to replicating domains in CHO9 interphase nuclei. Chromosome Res 22:463–481
20. Schermelleh L, Heintzmann R, Leonhardt H (2010) A guide to super-resolution fluorescence microscopy. J Cell Biol 190:165–175
21. Reindl J, Drexler GA, Girst S, Greubel C, Siebenwirth C, Drexler SE, Dollinger G, Friedl AA (2015) Nanoscopic exclusion between Rad51 and 53BP1 after ion irradiation in human HeLa cells. Phys Biol 12:066005
22. Reindl J, Girst S, Walsh DW, Greubel C, Schwarz B, Siebenwirth C, Drexler GA, Friedl AA, Dollinger G (2017) Chromatin organization revealed by nanostructure of irradiation induced γH2AX, 53BP1 and Rad51 foci. Sci Rep 7:40616

23. Natale F, Rapp A, Yu W, Maiser A, Harz H, Scholl A, Grulich S, Anton T, Hörl D, Chen W, Durante M, Taucher-Scholz G, Leonhardt H, Cardoso MC (2017) Identification of the elementary structural units of the DNA damage response. Nat Commun 8:15760
24. Lopez Perez R, Best G, Nicolay NH, Greubel C, Rossberger S, Reindl J, Dollinger G, Weber KJ, Cremer C, Huber PE (2016) Superresolution light microscopy shows nanostructure of carbon ion radiation-induced DNA double-strand break repair foci. FASEB J 30:2767–2776
25. Sisario D, Memmel S, Doose S, Neubauer J, Zimmermann H, Flentje M, Djuzenova CS, Sauer M, Sukhorukov V (2018) Nanostructure of DNA repair foci revealed by superresolution microscopy. FASEB J 32:6469–6477
26. Mladenov E, Kalev P, Anachkova B (2009) The complexity of double-strand break ends is a factor in the repair pathway choice. Radiat Res 171:397–404
27. Sheen MR, Kim SW, Jung JY, Ahn JY, Rhee JG, Kwon HM, Woo SK (2006) Mre11-Rad50-Nbs1 complex is activated by hypertonicity. Am J Physiol Ren Physiol 291:F1014–F1020
28. van de Linde S, Löschberger A, Klein T, Heidbreder M, Wolter S, Heilemann M, Sauer M (2011) Direct stochastic optical reconstruction microscopy with standard fluorescent probes. Nat Protoc 6:991–1009
29. Wolter S, Löschberger A, Holm T, Aufmkolk S, Devauballe MC, van de Linde S, Sauer M (2012) rapidSTORM: accurate, fast open-source software for localization microscopy. Nat Methods 9:1040–1041
30. Levet F, Hosy E, Kechkar A, Butler C, Beghin A, Choquet D, Sibarita JB (2015) SR-Tesseler: a method to segment and quantify localization-based super-resolution microscopy data. Nat Methods 12:1065–1071
31. Aurenhammer F (1991) Voronoi diagrams—a survey of a fundamental geometric data structure. ACM Comput Surv 23:345–405
32. Chamma I, Levet F, Sibarita JB, Sainlos M, Thoumine O (2016) Nanoscale organization of synaptic adhesion proteins revealed by single-molecule localization microscopy. Neurophotonics 3:041810. https://doi.org/10.1117/1.NPh.3.4.041810
33. Hadipour-Lakmehsari S, Driouchi A, Lee SH, Kuzmanov U, Callaghan NI, Heximer SP, Simmons CA, Yip CM, Gramolini AO (2019) Nanoscale reorganization of sarcoplasmic reticulum in pressure-overload cardiac hypertrophy visualized by dSTORM. Sci Rep 9:7867. https://doi.org/10.1038/s41598-019-44331-y
34. Martinière A, Fiche JB, Smokvarska M, Mari S, Alcon C, Dumont X, Hematy K, Jaillais Y, Nollmann M, Maurel C (2019) Osmotic stress activates two reactive oxygen species pathways with distinct effects on protein nanodomains and diffusion. Plant Physiol 179:1581–1593
35. Pereira PM, Albrecht D, Culley S, Jacobs C, Marsh M, Mercer J, Henriques R (2019) Fix your membrane receptor imaging: actin cytoskeleton and CD4 membrane organization disruption by chemical fixation. Front Immunol 10:675. https://doi.org/10.3389/fimmu.2019.00675
36. Costes SV, Chiolo I, Pluth JM, Barcellos-Hoff MH, Jakob B (2010) Spatiotemporal characterization of ionizing radiation induced DNA damage foci and their relation to chromatin organization. Mutat Res 704:78–87
37. de Berg M, van Kreveld M, van Overmars M, Schwarzkopf O (2000) Computational geometry: algorithms and applications. Springer, Berlin, pp 2–8
38. Braden B (1986) The surveyor's area formula. Coll Math J 17:326–337
39. Burma S, Chen B, Murphy M, Kurimasa A, Chen D (2001) ATM phosphorylates histone H2AX in response to DNA double-strand breaks. J Biol Chem 276:42462–42467
40. Solier S, Sordet O, Kohn KW, Pommier Y (2009) Death receptor-induced activation of the chk2- and histone H2AX-associated DNA damage response pathway. Mol Cell Biol 29:68–82
41. de Feraudy S, Revet I, Bezrookove V, Feeney L, Cleaver JE (2010) A minority of foci or pan-nuclear apoptotic staining of gamma-H2AX in the S phase after UV damage contain DNA double-strand breaks. Proc Natl Acad Sci USA 107:6870–6875. https://doi.org/10.1073/pnas.1002175107
42. Meyer B, Voss KO, Tobias F, Jakob B, Durante M, Taucher-Scholz G (2013) Clustered DNA damage induces pannuclear H2AX phosphorylation mediated by ATM and DNA-PK. Nucleic Acids Res 41:6109–6118
43. Mungunsukh O, Griffin AJ, Lee YH, Day RM (2010) Bleomycin induces the extrinsic apoptotic pathway in pulmonary endothelial cells. Am J Physiol Lung Cell Mol Physiol 298:L696–L703
44. Cook PJ, Ju BG, Telese F, Wang X, Glass CK, Rosenfeld MG (2009) Tyrosine dephosphorylation of H2AX modulates apoptosis and survival decisions. Nature 458:591–596
45. Dong Y, Xiong M, Duan L, Liu Z, Niu T, Luo Y, Wu X, Xu C, Lu C (2014) H2AX phosphorylation regulated by p38 is involved in Bim expression and apoptosis in chronic myelogenous leukemia cells induced by imatinib. Apoptosis 19:1281–1292
46. Costes SV, Boisière A, Ravani S, Romano R, Parvin B, Barcellos-Hoff MH (2006) Imaging features that discriminate between foci induced by high- and low-LET radiation in human fibroblasts. Radiat Res 165:505–515
47. McManus KJ, Hendzel MJ (2005) ATM-dependent DNA damage-independent mitotic phosphorylation of H2AX in normally growing mammalian cells. Mol Biol Cell 16:5013–5025
48. Pron G, Mahrour N, Orlowski S, Tounekti O, Poddevin B, Belehradek J Jr, Mir LM (1999) Internalisation of the bleomycin molecules responsible for bleomycin toxicity: a receptor-mediated endocytosis mechanism. Biochem Pharmacol 57:45–56
49. Chen J, Chen Y, He Q (2012) Action of bleomycin is affected by bleomycin hydrolase but not by caveolin-1. Int J Oncol 41:2245–2252
50. Olive PL, Banath JP (1993) Detection of DNA double-strand breaks through the cell cycle after exposure to X-rays, bleomycin, etoposide and ^{125}IdUrd. Int J Radiat Biol 64:349–358
51. Burger RM, Peisach J, Horwitz SB (1981) Activated bleomycin: a transient complex of drug, iron, and oxygen that degrades DNA. J Biol Chem 256:11636–11644
52. Grigaravicius P, Rapp A, Greulich KO (2009) A direct view by immunofluorescent comet assay (IFCA) of DNA damage induced by nicking and cutting enzymes, ionizing ^{137}Cs radiation, UV-A laser microbeam irradiation and the radiomimetic drug bleomycin. Mutagenesis 24:191–197
53. Phillips JE, Corces VG (2009) CTCF: master weaver of the genome. Cell 137:1194–1211
54. Szilard RK, Jacques PE, Laramée L, Cheng B, Galicia S, Bataille AR, Yeung M, Mendez M, Bergeron M, Robert F et al (2010) Systematic identification of fragile sites via genome-wide location analysis of gamma-H2AX. Nat Struct Mol Biol 17:299–305
55. Seo J, Kim SC, Lee HS, Kim JK, Shon HJ, Salleh NL, Desai KV, Lee JH, Kang ES, Kim JS, Choi JK (2012) Genome-wide profiles of H2AX and γ-H2AX differentiate endogenous and exogenous DNA damage hotspots in human cells. Nucleic Acid Res 40:5965–5974
56. Nouspikel T, Hanawalt PC (2002) DNA repair in terminally differentiated cells. DNA Repair 1:59–75
57. Turinetto V, Giachino C (2015) Multiple facets of histone variant H2AX: a DNA double-strand-break marker with several biological functions. Nucleic Acids Res 43:2489–2498
58. Hausmann M, Wagner E, Lee JH, Schrock G, Schaufler W, Krufczik M, Papenfuß F, Port M, Bestvater F, Scherthan H (2018) Super-resolution localization microscopy of radiation-induced

histone H2AX-phosphorylation in relation to H3K9-trimethylation in HeLa cells. Nanoscale 10:4320–4331
59. Blackford AN, Jackson SP (2017) ATM, ATR, and DNA-PK: the trinity at the heart of the DNA damage response. Mol Cell 66:801–817
60. Salzano M, Sanz-García M, Monsalve DM, Moura DS, Lazo PA (2015) VRK1 chromatin kinase phosphorylates H2AX and is required for foci formation induced by DNA damage. Epigenetics 10:373–383
61. Chowdhury D, Keogh MC, Ishii H, Peterson CL, Buratowski S, Lieberman J (2005) gamma-H2AX dephosphorylation by protein phosphatase 2A facilitates DNA double-strand break repair. Mol Cell 20:801–809
62. Nakada S, Chen GI, Gingras AC, Durocher D (2008) PP4 is a gamma H2AX phosphatase required for recovery from the DNA damage checkpoint. EMBO Rep 9:1019–1026
63. Svetlova M, Solovjeva L, Nishi K, Nazarov I, Siino J, Tomilin N (2007) Elimination of radiation-induced gamma-H2AX foci in mammalian nucleus can occur by histone exchange. Biochem Biophys Res Commun 358:650–654
64. Jung EJ, Kim CW, Kim DR (2008) Cytosolic accumulation of gammaH2AX is associated with tropomyosin-related kinase A-induced cell death in U2OS cells. Exp Mol Med 40:276–285